ACS APPLIED MATERIALS & INTERFACES

www.acsami.org

Research Article

Heterogeneous Structure of Sn/SnO_2 Constructed via Phase Engineering for Efficient and Stable CO_2 Reduction

Zhipeng Liu,[‖] Chang Liu,[‖] Suhua Mao, and Xiaoxi Huang*

Cite This: https://doi.org/10.1021/acsami.2c18522

Read Online

ACCESS | Metrics & More | Article Recommendations | Supporting Information

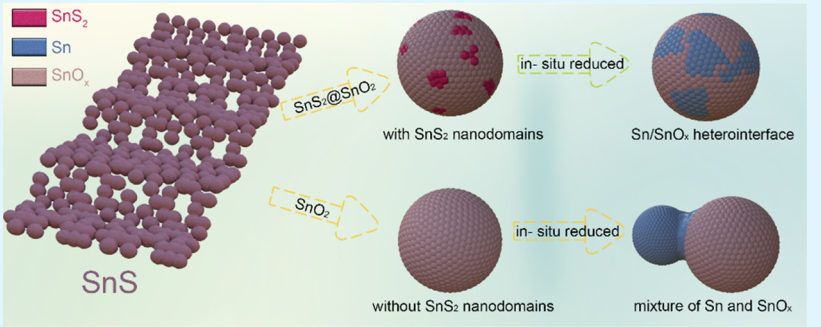

ABSTRACT: The electrochemical carbon dioxide reduction reaction (CO_2RR) catalyzed by Sn-based materials shows great potential for CO_2-to-formate conversion. The presence of tin species with different oxidation states can promote the catalytic performance, most likely due to the interfaces of metallic and oxide phases that induce a synergistic effect. Therefore, it is desirable yet challenging to synthesize a hybrid catalyst with abundant active heterogeneous interfaces. Herein, we synthesize a hybrid catalyst constructed by decorating nanosized SnS_2 in the SnO_2 matrix. The uniformly distributed SnS_2 nanoparticles are first reduced to metallic tin, which assists in the generation of abundant Sn/SnO_2 heterogeneous interfaces under the *in situ* reduction process. Because of the electronic modulation at the heterogeneous interfaces, the resulting catalyst delivers a high current density of 200 mA·cm^{-2} at −0.86 V vs RHE, and the performance is stable for over 20 h. This work suggests a potentially powerful interface engineering strategy for the development of high-performance electrocatalysts for the CO_2RR.

KEYWORDS: *CO_2 reduction reaction, tin dioxide, formate, in situ reconstruction, heterostructure*

1. INTRODUCTION

The global environmental concern and energy crisis have accelerated the development of sustainable energy.[1] In the past decades, electrocatalysis has emerged as a promising technology for renewable energy conversion and storage.[2,3] Among the diverse proposed methods, the electrochemical carbon dioxide reduction reaction (CO_2RR) is an elegant solution for sustainable and renewable energy supply, which can fix atmospheric CO_2 and produce fuels or industrially important chemicals, thereby closing the carbon cycle.[4−7] However, the energy conversion efficiency of the CO_2RR is usually impeded by the following aspects: the CO_2 molecule has stable carbon oxygen bonds that require high activation energy to break; multiple reaction routes and multiple proton/electron transfer steps are involved during the CO_2RR process; and the reaction is accompanied with hydrogen evolution, resulting in poor selectivity.[8,9] Therefore, efficient catalysts are essential to achieve the goal of carbon neutrality based on the electrochemical CO_2RR.[6,10]

Formic acid or formate is regarded as a suitable target product with high economic viability and widely applied in the realms of both industries and agriculture.[11,12] Previous studies demonstrate that the most appealing catalysts for formate production are represented by main group metals and their compounds,[8,13−16] possibly due to their non-close-packed crystal structures.[17] In particular, Sn-based materials have attracted substantial interest since 1980s due to their low toxicity and earth-abundant features.[18−21] However, the sporadic Faraday efficiencies (ranging from 10 to 90%) and undesirable intrinsic activity still hinder their application, whereas the uncontrollable evolution of Sn species during the CO_2RR process is proposed as the primary issue.[13,22−25] Generally, metallic Sn is prone to oxidation in air, and the oxide shell contributes to catalytic activity.[26,27] Nevertheless, the oxide shell tends to be reduced since the operating potential for the CO_2RR is more negative than its standard

Received: October 16, 2022
Accepted: January 11, 2023

redox potentials. This reduction process is accompanied by structural reconstruction and produces diverse Sn species depending on the reduction potential, which leads to uncontrollable variation in catalytic performance toward the CO_2RR.[28−30]

Of note, a substantial oxide phase persists in SnO_2 electrodes during cathodic reactions as manifested by *in situ* observations.[30,31] Consequently, multivalent Sn species including metallic Sn and its oxides are usually involved in SnO_2-based catalysts, which can contribute synergistic effects for the catalytic process.[32−34] In particular, the metallic Sn and SnO_2 derived from identical precursors tend to join with each other, forming robust heterogeneous interfaces at the grain boundaries. Because of the unique local coordination environment at interfaces, the electronic structure of Sn atoms can be altered, thereby influencing the intrinsic catalytic activity.[35−40] In this regard, constructing a heterostructure of metallic Sn and SnO_2 with abundant interfacial boundaries is promising to fabricate an efficient catalyst for CO_2-to-formate conversion, wherein a uniform distribution of Sn in the SnO_2 matrix is essential. However, aggregation of metallic Sn *in situ* derived from SnO_2 is thermodynamically more favorable, and modulating the dispersion of Sn in the nanoscale remains challenging.

To this end, we propose a hybrid precatalyst constructed by doping SnS_2 in SnO_2 uniformly. Different coordination structures of Sn induce discrepant reduction barriers, and SnS_2 is reduced first, forming a number of metallic nanodomains embedded in the SnO_2 matrix. These metallic nanodomains serve as nucleation sites for further generation of metallic tin, which lead to uniform distribution of metallic Sn and help fabricate abundant Sn/SnO_2 heterogeneous interfaces. Due to the electronic modulation at the interface, the *in situ* reconstructed catalyst exhibits a remarkable catalytic performance toward the CO_2RR with a high selectivity of formate over a wide potential range, surpassing the pristine SnO_2 electrocatalyst. Moreover, it delivers high selectivity and robust stability under industrially applicable current density in a flow cell.

2. EXPERIMENTAL SECTION

2.1. Synthesis of SnS_2@SnO_2 and SnO_2. First, 2 mmol stannous chloride ($SnCl_2$) was dissolved in a 20 mL aqueous solution containing 0.3 g of polyetherimide (PEI), 3 mL of acetic acid (HOAc), and 0.5 mmol citic acid (CA). The solution was mildly stirred for 30 min at 50 °C. Afterward, 2 mmol thioacetamide (TAA) was dissolved in 10 mL of deionized water and slowly added to the above-mentioned solution under vigorous stirring to form a uniform solution. The solution was then transferred into an autoclave and heated at 100 °C for 24 h. After cooling to room temperature naturally, the solid product was collected via centrifugation, rinsed with deionized water and ethanol several times, and dried at 60 °C in a vacuum oven. The as-obtained black powder was denoted as a SnS precursor. The SnS precursor was then converted into SnS_2@SnO_2 via annealing in a muffle furnace at 550 °C for 2 h with a heating rate of 5 °C·min^{-1}. To investigate the structural evolution during thermal treatment, 1 and 3 h heating times were also adopted.

For comparison purposes, SnO_2 was synthesized via annealing the SnS precursor at an elevated temperature of 800 °C for 2 h with the same heating rate to oxidize all tin sulfide species.

2.2. Material Characterization. Scanning electron microscopy (SEM) images were collected using a field emission SEM instrument (Zeiss SIGMA or JEOL JSM-IT800) at 10 kV acceleration voltage. Transmission electron microscopy (TEM) images were collected on a JEOL JEM-2100F microscope at 200 kV equipped with an energy dispersive X-ray (EDS) spectrometer (INCA). The crystallographic information of the catalysts was measured on a Bruker D8 Advanced X-ray diffractometer with Cu Kα radiation (λ = 0.15418 nm) at 40 kV and 40 mA. The surface chemical state of the catalysts was investigated on a ThermoFisher Nexsa X-Ray photoelectron spectrometer with Al Kα radiation ($h\nu$ = 1486.6 eV).

2.3. Working Electrode Preparation and Electrochemical CO_2RR Measurements. To prepare the working electrode, 10 mg of electrocatalyst and 80 μL of Nafion solution (5 wt %) were added to 1 mL of ethanol and ultrasonicated to prepare homogeneous catalyst ink. Then, 500 μL of catalyst ink was sprayed on carbon paper with a working area of 1 × 1 cm^2, and the resulting electrode was dried in a vacuum oven at 60 °C for 24 h.

The electrochemical CO_2RR measurements were conducted in a gas-tight two-compartment H-cell separated using an ion exchange membrane. Next, 0.5 M $KHCO_3$ solution was utilized as a catholyte, which was bubbled with CO_2 before and during the CO_2RR test (10 sccm) to ensure that CO_2 is saturated in the electrolyte. The catholyte was also stirred at a rate of 300 rpm. The electrochemical measurement was conducted using a typical three-electrode system connected to a potentiostat (CHI 660E). A Ag/AgCl (3 M KCl) electrode and a piece of platinum foil were utilized as the reference and counter electrodes, respectively. The carbon paper loaded with the catalyst was used as the working electrode. The potential of the working electrode was held at −1.1 V vs RHE for 1 h to reduce the catalyst before evaluation of the CO_2RR performance. Subsequently, the electrolyte was replaced, and the chronoamperometry curve was recorded for 2 h under a static potential ranging from −0.8 to −1.4 V vs RHE to analyze the products of the CO_2RR. The product analysis was performed according to our previous report.[41,42] In the process of bulk electrolysis, the gaseous products were directly vented into the sampling loop of an online gas chromatograph (Angilent 7890 B) at 20 min interval for quantification. After electrolysis, 300 μL of the catholyte was sampled and analyzed by nuclear magnetic resonance (NMR) spectroscopy (JEOL JEM-ECZ400S/L1) using DMSO as an internal standard.

To evaluate the electrochemically active surface area (ECSA), cyclic voltammetry (CV) measurements were conducted in the potential range from 0.1 to 0.3 V vs RHE at several scan rates between 20 and 180 mV·s^{-1} with 20 mV·s^{-1} interval. The electrode potential was converted to the reversible hydrogen electrode scale following $E(\mathrm{RHE}) = E(\mathrm{Ag/AgCl}) + 0.210 + 0.0591 \times \mathrm{pH}$ without *i-R* compensation. The TOFs of the electrocatalysts were estimated based on the mass loading of electrocatalysts on carbon paper according to the following equation[43]

$$\mathrm{TOF} = \frac{j}{n \times F \times L}$$

where j is the partial current corresponding to formate, n = 2 is the number of transferred electrons, F(96485.3 C·mol^{-1}) is the Faraday constant, and L (mole) is the number of active sites under the assumption that all tin atoms in the catalyst are active.

2.4. CO_2RR in a Flow Cell. The performance of the CO_2RR at high current density was evaluated in a flow cell as described in our previous report.[41] To prepare the gas diffusion electrode, 1 mL of catalyst ink was sprayed on a 2.5 × 2 cm^2 carbon paper and 2 × 0.5 cm^2 of the carbon paper was exposed to the electrolyte. A Pt foil and a solid Ag/AgCl electrode (GaossUnion) were used as the counter electrode and reference electrode, respectively. The flow rate of CO_2 gas was set as 30 sccm during the electrolysis. 1 M $KHCO_3$ or 1 M KOH solution was used as the electrolyte. Electrochemical impedance spectra were recorded with frequencies ranging from 10 kHz to 0.01 Hz at a potential of 0.1 V vs RHE, and the impedance data were fitted according to a simplified Randles model. Electrochemical test data in the flow cell configuration were presented with 80% i-R compensation.

2.5. Density Functional Theory (DFT) Calculations. The spin polarized DFT calculations were performed using MedeA VASP (Vienna Ab initio Simulation Package).[44−46] The generalized gradient approximation Perdew−Burke−Ernzerhof (GGA-PBE) exchange

https://doi.org/10.1021/acsami.2c18522
ACS Appl. Mater. Interfaces XXXX, XXX, XXX−XXX

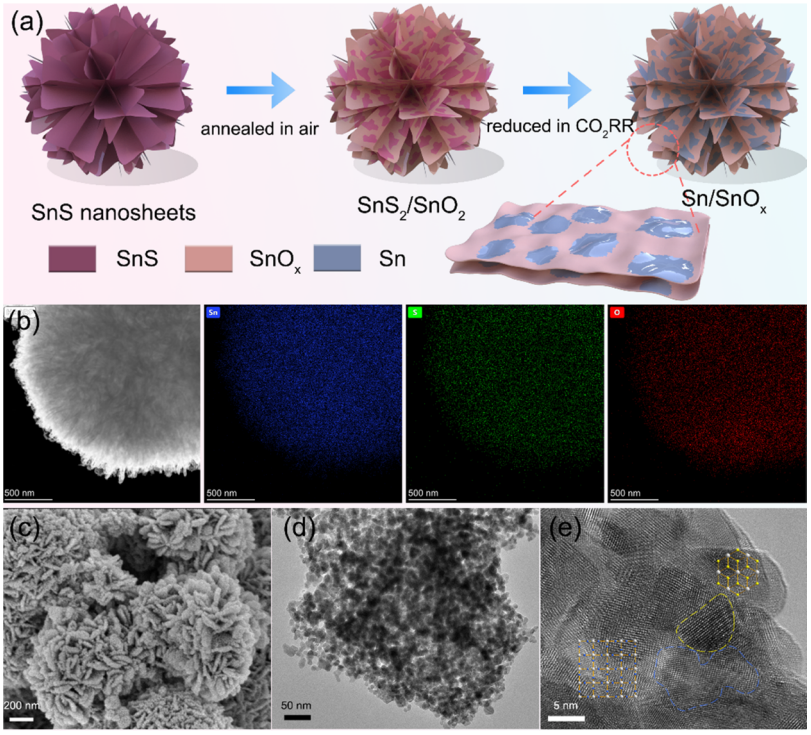

Figure 1. (a) Schematic illustration of the synthesis process of the SnS_2@SnO_2 precatalyst and the subsequent *in situ* reduction process to generate hybrid Sn-based catalysts with many metal/oxide interfacial boundaries. (b) EDS elemental mappings, and (c) SEM, (d) TEM, and (e) HRTEM images of SnS_2@SnO_2 after annealing the SnS precursor for 2 h.

correlation functional was selected to described the interactions.[47] The plane wave cutoff energy was set as 400 eV. The DFT + D3 approach of S. Grimme with zero damping was used to handle van der Waals interactions.[48] The γ-centered k point was sampled with a k-spacing of 0.3 $Å^{-1}$. For geometry optimization, the convergence criteria of 1.0×10^{-5} eV and 0.01 eV·$Å^{-1}$ were used for the electronic self-consistent iteration and the ionic relaxations. The vacuum space between the slabs is ~18 Å.

To calculate the free energy profile of CO_2-to-formate conversion, the following elementary steps were considered

$$CO_2 + H^+ + e^- + * = *OCHO \quad (1)$$

$$*OCHO + H^+ + e^- = * + HCOOH \quad (2)$$

where * represents the catalyst slab. The free energy changes of each step were calculated based on the following equations

$$\Delta G(1) = G(*OCHO) - G(CO_2) - G(H^+ + e^-) - G(*)$$

$$\Delta G(2) = G(*) + G(HCOOH) - G(*OCHO) - G(H^+ + e^-)$$

The value of $0.5G(H_2)$ was used to replace $G(H^+ + e^-)$ based on a computational hydrogen electrode (CHE) model. The results of $G(CO_2)$ = −22.79 eV, $G(H_2)$ = −6.94 eV, and $G(HCOOH)$ = −29.71 eV were obtained from the previous publications.[49,50] After calculating the total energy of *OCHO from DFT, the Gibbs free energy was further calculated using the VASPKIT package at 298.15 K.[51]

3. RESULTS AND DISCUSSION

3.1. Synthesis and Characterization of SnS_2@SnO_2. A uniform hybrid precatalyst of SnS_2 and SnO_2 (denoted as SnS_2@SnO_2) was obtained via a two-step synthetic approach as illustrated in Figure 1a. Tin monosulfide (SnS) with a nanoflower morphology (Figure S1) was first fabricated through a hydrothermal method and utilized as a precursor, which was gradually converted into SnS_2@SnO_2 by annealing in air. The time-dependent XRD results (Figure S2) indicate that SnS is consumed at the initial period of annealing, as evidenced by the disappearance of the representative diffraction signals corresponding to SnS. Meanwhile, SnO_2 and SnS_2 are synchronously obtained and SnS_2 is further converted into SnO_2 as calcination proceeds. The EDS elemental mappings of the samples obtained at different annealing times reveal a homogeneous distribution of Sn, S, and O along the nanosheets (Figures 1b and S3), suggesting that SnS_2 is uniformly doped in SnS_2@SnO_2. Moreover, the proportion of sulfide species gradually decreases as the reaction time was prolonged (Table S1), and a blue shift of Sn 3d binding energy was observed in the XPS spectra (Figure S4). The time-dependent SEM images indicate that the initial nanoflower morphology of the SnS precursor was well retained (Figures 1c and S5) throughout the calcination process, but the surface of the nanosheets became coarse. In accordance, the TEM images (Figures 1d, S1, and S6) manifest that the nanosheet is fragmented into nanoparticles with a diameter of a few nanometers. Cracks and chaps were observed between the nanoparticles, which are probably correlated with the volume contraction involved in the conversion from SnS to SnO_2.[52,53]

Based on the above-mentioned characterization results, the annealing process enables the construction of a heterogeneous structure with a uniform distribution of SnS_2 and SnO_2. Moreover, it is expected that the SnO_2 and SnS_2 nanoparticles have intimate connection between each other since they are simultaneously derived from an identical SnS precursor. The proportion of SnS_2 is about 10% in SnS_2@SnO_2 according to the EDS analysis. The corresponding TEM image (Figure 1e) reveals that the sample is composed of nanocrystals with a diameter of less than 20 nm. Nanodomains with lattices

https://doi.org/10.1021/acsami.2c18522
ACS Appl. Mater. Interfaces XXXX, XXX, XXX−XXX

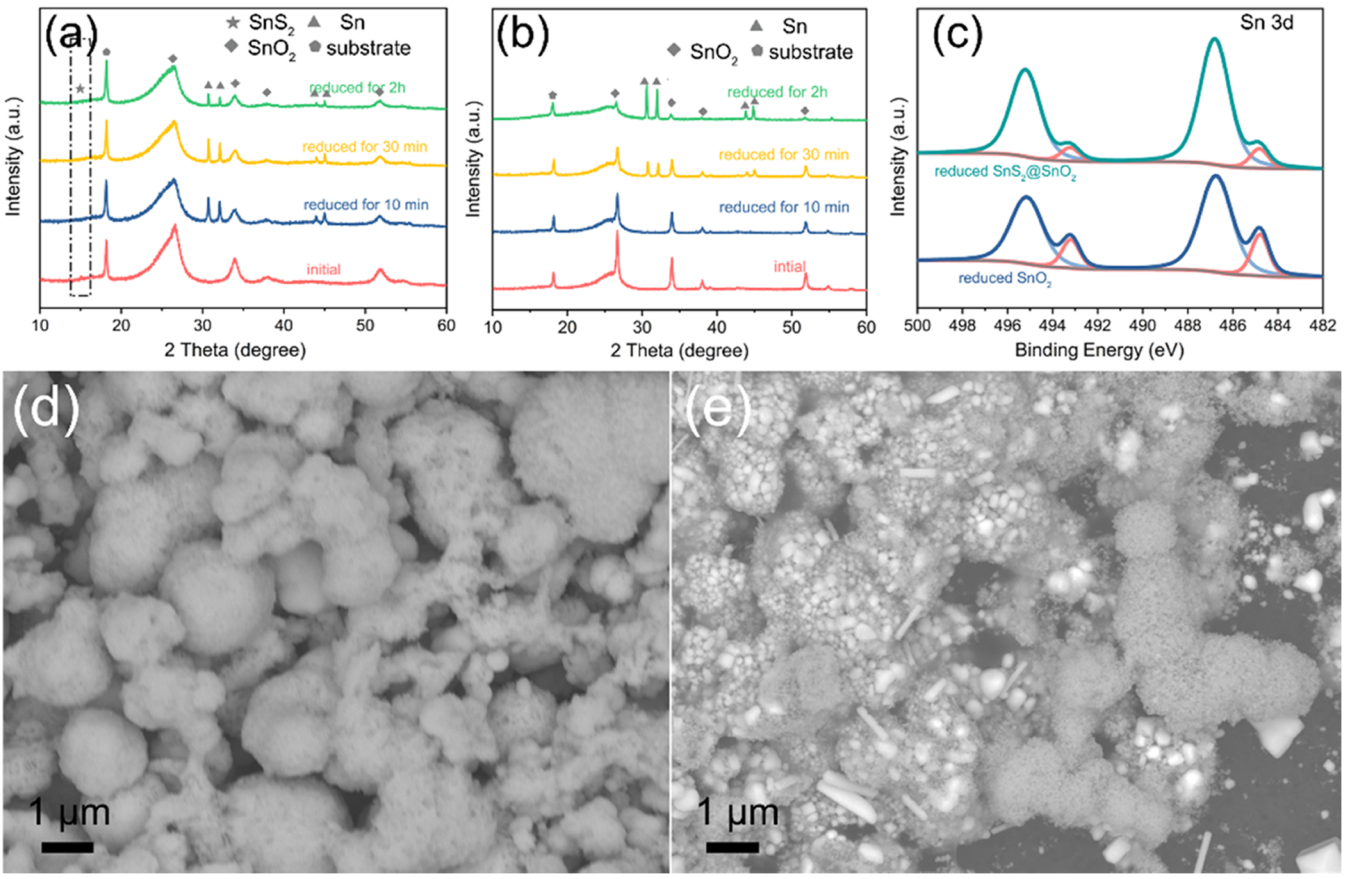

Figure 2. XRD patterns of (a) SnS_2@SnO_2 and (b) SnO_2 electrodes after reducing for various times. The diffraction peaks corresponding to SnS_2, SnO_2, Sn, and carbon paper substrates are marked in the graph. (c) XPS spectra of reduced SnS_2@SnO_2 and SnO_2. SEM images of reduced (d) SnS_2@SnO_2 and (e) SnO_2 electrodes collected via a backscattered electron detector.

indexed to the (100) plane of SnS_2 (circled with a yellow dash line) were embedded in the SnO_2 matrix (circled with a blue dash line), and different lattices are interwoven with each other (Figure 1e). Aside from SnS_2@SnO_2, a control sample was synthesized at 800 °C to oxidize the material thoroughly. The resulting material (denoted as SnO_2) has a similar tin oxidation number compared with that of SnS_2@SnO_2, based on Sn 3d XPS analysis (Figure S4a). It is porous, based on the SEM observation, and only composed of tin dioxide according to the XRD measurement (Figure S7).

3.2. *In situ* Reconstruction of the Catalysts. Generally, the CO_2RR is conducted under a cathodic potential more negative than the standard redox potential of Sn/SnO_2; therefore, generation of metallic Sn is inevitable during the electrolysis.[54,55] Because of the distinct coordination structures of SnS_2 and SnO_2, they could have different reduction energy barriers. The XRD results suggest that SnS_2 in SnS_2@SnO_2 is fully reduced as the characteristic peak at ∼15° disappears within 10 min at −1.1 V vs RHE (Figure 2a) and the S signal is not detected in the XPS spectrum (Figure S8). Meanwhile, the peaks attributed to SnO_2 decrease slightly and diffraction peaks correlated with metallic Sn increase. Notably, the proportion of metallic Sn is almost constant in SnS_2@SnO_2 for a prolonged reaction time at −1.1 V, indicating that SnO_2 species were not further reduced. In contrast, the metallic Sn in the control SnO_2 sample appears after 30 min of reduction, and the material is unstable, as the amount of metallic Sn continues to increase significantly after 2 h of reduction (Figure 2b). Consistent with the XRD results, a minor peak correlated with metallic Sn species arises in both XPS spectra of reduced SnS_2@SnO_2 and SnO_2 (Figure 2c), and the proportions of metallic Sn generated from SnS_2@SnO_2 and SnO_2 are ∼ 10% and ∼20%, respectively. Based on these results, we conclude that both SnS_2@SnO_2 and SnO_2 precatalysts are converted into new materials composed of different ratios of metallic Sn and SnO_2 during the CO_2RR process.

Next, we aim to explore the distribution and microstructures of Sn and SnO_2 on the electrode after the CO_2RR via electron microscopy. For SEM observations, aside images obtained via a typical secondary electrons detector (SED), a backscattered electron detector (BED) was used to take images, which are sensitive to the composition of the sample and capable of distinguishing the compositional difference. In terms of SnS_2@SnO_2, the shape of the nanoflower is slightly destroyed in the reduction process (Figure S9a), indicating significant structural reconstruction. Of note, the brightnesses in different positions of the SEM image obtained with the BED are similar (Figure 2d), suggesting that distribution of metallic tin is uniform in SnS_2@SnO_2 after reduction. On the contrary, a slew of randomly distributed metallic Sn nanoparticles is observed via backscattered electron imaging (Figure 2e). The elemental mappings further confirm that the brighter areas have less oxygen contents (Figure S10). These results prove that metallic Sn derived from SnO_2 experiencing an identical reduction process tends to agglomerate and form large particles.

TEM was used to investigate the structure in more detail. Regarding SnS_2@SnO_2, the resultant still consists of nano-

https://doi.org/10.1021/acsami.2c18522
ACS Appl. Mater. Interfaces XXXX, XXX, XXX−XXX

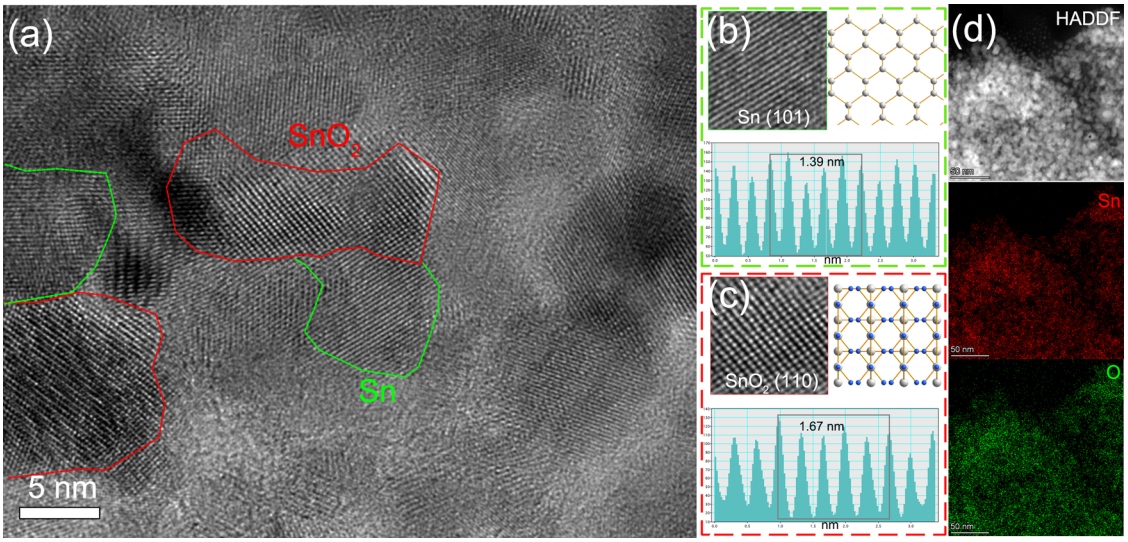

Figure 3. (a) HRTEM image of reduced SnS_2@SnO_2 and (b, c) zoom-in view of the selected regions. (d) EDS elemental mapping of the reduced SnS_2@SnO_2.

particles with a similar size to that of the initial precatalyst (Figure S11). The HRTEM image (Figure 3a−c) reveals distinct lattice fringes as marked with green and red dash lines, which can be indexed to the (101) planes of Sn and the (110) planes of SnO_2, respectively. In addition, the distributions of tin and oxygen elements are uniform (Figure 3d). Therefore, it is expected that a plenty of heterogeneous interfaces are generated between the boundaries of metallic Sn and SnO_2. In contrast, for the sample derived from the SnO_2 precatalyst, isolated tin nanoparticles with a larger size are observed (Figure S12).

Compared with pure SnO_2, the unique structure with abundant Sn/SnO_2 interfaces derived from SnS_2@SnO_2 is likely related with the presence of SnS_2 nanodomains, leading to different reduction mechanisms between SnS_2@SnO_2 and SnO_2. Given the fact that SnS_2 is uniformly distributed along the SnO_2 matrix after thermal annealing, this metallic Sn reduced from SnS_2 can incorporate with SnO_2 lattices intimately and form abundant heterogeneous interfaces, while in the case of SnO_2, the reduction occurs stochastically and segregation of metallic Sn is thermodynamically more favorable compared with uniform distribution.

3.3. Electrochemical Measurements. To check whether the distinct structures derived from SnS_2@SnO_2 and SnO_2 precatalysts would have noticeable impacts on their CO_2RR performance, the catalytic activity and selectivity were compared in a H-type cell. The electrolysis was conducted with a potentiostatic measurement. The gas and liquid products were quantitatively identified by online gas chromatography (GC) and ^{1}H nuclear magnetic resonance (NMR) spectroscopy, respectively. For both catalysts, H_2 and CO were collected as gas products and formate is the only liquid product (Figure S13). The Faraday efficiencies (FEs) of these products are illustrated in Figure 4a,b. In the case of SnS_2@SnO_2, the FE of formate ($FE_{formate}$) is over 80% under a wide potential range from −1.0 to −1.4 V vs RHE and approaches the maximum value of 90% at −1.1 V. Compared with SnS_2@SnO_2, the $FE_{formate}$ in SnO_2 is apparently dependent on the applied potential values. A volcano-shaped correlation was observed with a maximum FE reaching ∼75% at −1.0 V, which is typically found in many Tin-based electrocatalysts (Figure S14).

In addition to the superior selectivity, the catalytic activity of SnS_2@SnO_2 is significantly higher than that of SnO_2. The partial current density (Figure 4c) for formate in SnS_2@SnO_2 is approximately 2 times that in SnO_2 under various potentials. Of note, SnS_2@SnO_2 reveals a comparable ECSA to that of SnO_2 (Figures 4d and S15), but its turnover frequency (TOFs, Figure 4e) is substantially larger, suggesting that SnS_2@SnO_2 has higher intrinsic catalytic activity toward the CO_2RR. Considering that both SnO_2 and CO_2 species can be reduced on the electrode and these reactions compete with each other, the presence of highly active sites is favorable to accelerate the electron transfer through the CO_2RR route, thereby suppressing the self-reduction of SnO_2. Based on the time-dependent XRD patterns in Figure 2a, SnS_2@SnO_2 is converted into Sn@SnO_2 quickly at the beginning of the CO_2 electrolysis and remains relatively stable afterward. As a result, after the initial activation process, the observed stable current density under a CO_2 atmosphere is due to CO_2 reduction, instead of catalyst reduction, which is also confirmed by stable product selectivity (Figure S16a). A fluctuant i−t curve and variable selectivity are obtained in SnO_2 (Figure S16b). In addition, more metallic Sn is produced by reducing SnS_2@SnO_2 in the absence of CO_2 compared with that reduced under CO_2RR conditions (Figure S16c,d). Combined with the aforementioned XRD results, it is deduced that further reduction of SnO_2 is suspended in the case of SnS_2@SnO_2 as the CO_2RR is predominate. The active sites, namely, the heterogeneous Sn/SnO_2 interfaces, were well retained after 5 h of CO_2RR electrolysis (Figure S17).

Economically competitive application of the CO_2RR technology needs to convert CO_2 at a high current density, whereas the reaction rate in a H-type cell is significantly limited by the low solubility of CO_2 in the electrolyte.[56−58] Therefore, the catalytic properties of these catalysts were further evaluated in a flow cell configuration. The LSV curves (Figures 4f and S18) reveal that the reaction rates in the flow cell are greatly accelerated both in KOH and $KHCO_3$ electrolytes. In particular, SnS_2@SnO_2 can deliver a current density of 100 mA·cm^{-2} in KOH and $KHCO_3$ at ∼−0.72 and −0.98 V vs RHE, respectively (Figure S19). In addition, the selectivity of

https://doi.org/10.1021/acsami.2c18522
ACS Appl. Mater. Interfaces XXXX, XXX, XXX−XXX

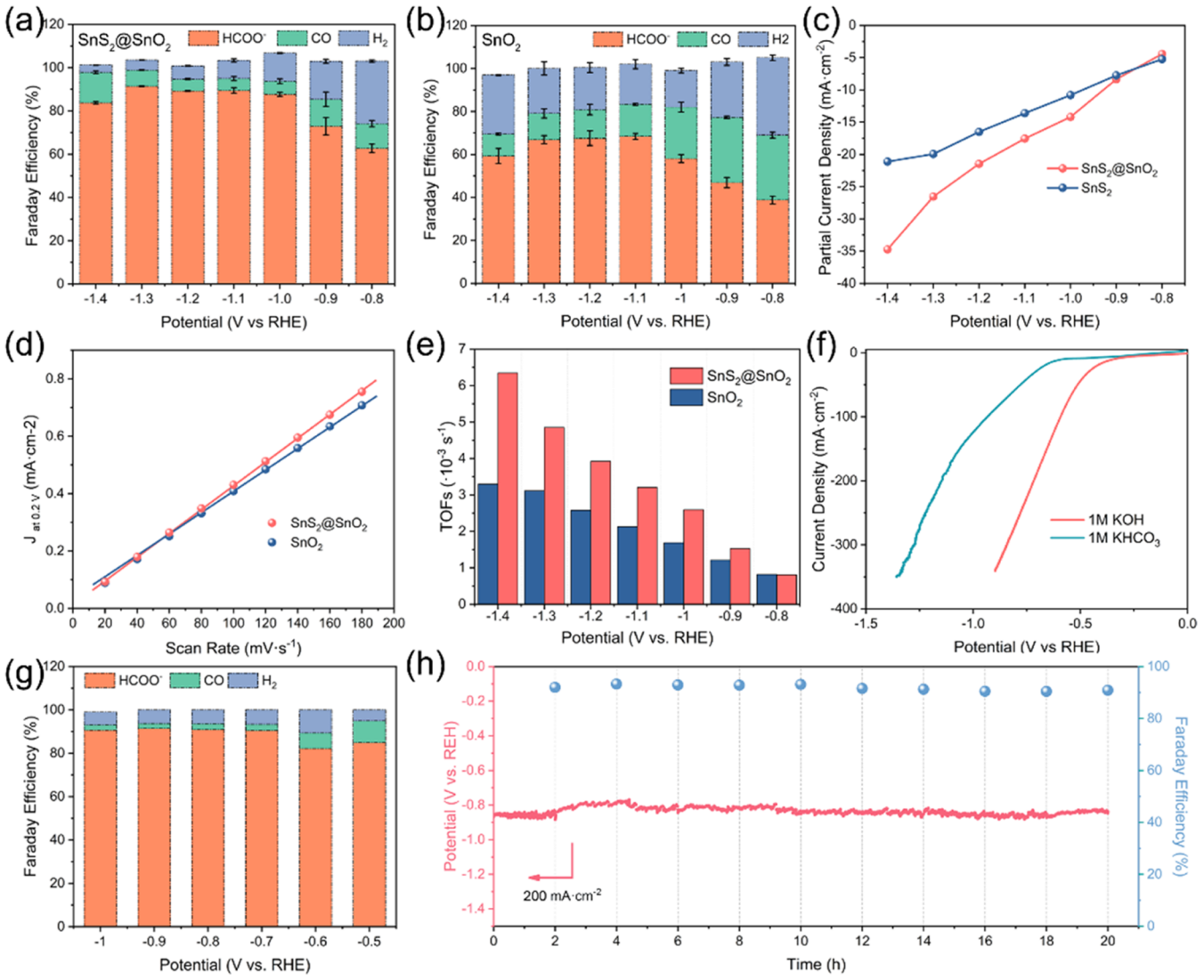

Figure 4. Faraday efficiency of (a) SnS_2@SnO_2 and (b) SnO_2 tested in a H-type cell in 0.5 M $KHCO_3$ and (c) corresponding $HCOO^-$ partial current density. (d) Linear regressions of differences in current density ($J = J_a - J_c$) at 0.2 V plotted against the scan rates for the estimation of the electrochemical surface area (ECSA). (e) TOFs of SnS_2@SnO_2 and SnO_2. (f) LSV curves of SnS_2@SnO_2 collected in a flow cell in 1 M $KHCO_3$ and 1M KOH. (g) FEs measured under various potentials and (h) stability test under a current density of 200 mA·cm^{-2} in 1 M KOH.

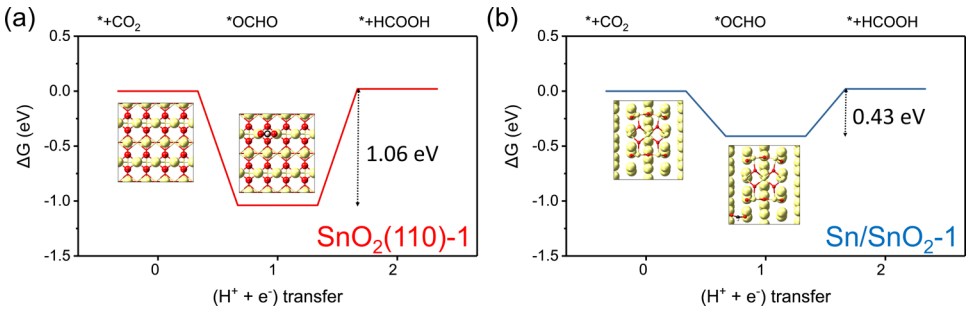

Figure 5. Calculated free energy profiles of the CO_2RR on (a) SnO_2 (110) surface and (b) Sn/SnO_2-1 interface. The insets show the optimized structures, and the yellow, red, black, and white balls represent the Sn, O, C, and H atoms, respectively. For SnO_2(110)-1, the surface atoms are displayed as CPK, while the bottom structures are shown as sticks. For Sn/SnO_2-1, the metallic tin is displayed as CPK and the SnO_x is shown as ball and sticks.

SnS_2@SnO_2 is enhanced in the flow cell, the FE corresponding to formate exceeds 90% at potential more negative than −0.7 V, and the hydrogen evolution is substantially suppressed (Figure 4g). Furthermore, galvanostatic curves collected under constant current densities of 200 mA·cm^{-2} (Figures 4h and S20) indicate a robust stability of SnS_2@SnO_2 with $FE_{formate}$ exceeding 90%. The products were inspected with 2 h interval, and the corresponding $FE_{formate}$ was stable for over 20 h. In

https://doi.org/10.1021/acsami.2c18522
ACS Appl. Mater. Interfaces XXXX, XXX, XXX−XXX

addition, the ratio of Sn and SnO_2 generated from reducing SnS_2@SnO_2 remains stable during the CO_2RR process in the flow cell based on the XRD measurement (Figure S21). Such a performance is quite competitive among the recently reported tin-based catalysts that can produce formate (listed in Table S2).

3.4. Discussion on the Catalytic Mechanism. On the basis of the aforementioned analysis, the final structures of SnS_2@SnO_2 and SnO_2 precatalysts after the CO_2RR process are different in terms of the distribution and proportion of metallic Sn. The continuous formation of large Sn aggregates in SnO_2 will act as a drag on the overall CO_2RR selectivity, as pure metallic tin generally favors the HER process. In terms of the SnS_2@SnO_2 precatalyst, metallic Sn nanodomains are uniformly embedded in the SnO_2 matrix, forming abundant heterogeneous interfaces between the boundaries, which we believe can contribute to better CO_2RR performance. To understand the mechanism, we use density functional theory (DFT) to calculate the free energy profile of CO_2-to-formate conversion on the SnO_2 (110) surface and Sn/SnO_2 model. As shown in Figure 5a, the conversion of CO_2 to *OCHO via the first (H^+ + e^-) transfer step is relatively easy, as the ΔG is negative. On the contrary, the free energy change of the system increases to 1.06 eV when *OCHO is converted into HCOOH on the SnO_2 (110) surface, indicating that the addition of the second (H^+ + e^-) pair is the rate-determining step. Interestingly, this value is reduced to 0.43 eV at the interface of Sn/SnO_2-1 (Figure 5b), implying that the sites around the *in situ* generated interface of metal/oxide could be more active for the CO_2-to-formate conversion compared with the initial SnO_2 phase. As the hydrogen evolution reaction is a major competing reaction for the CO_2RR in aqueous solution, the free energy change profile of the HER at the interface of Sn/SnO_2-1 is calculated. It is obvious that the ΔG of *H formation is positive (Figure S22), suggesting that the formation of *H is less favorable compared with that of *OCHO, which explains the high selectivity of formate. In addition to this interfacial structure, another Sn/SnO_2-2 structure was constructed by putting a tin cluster on the SnO_2(110) surface, and the calculated results also show that the elevated free energy change of the rate-limiting step is reduced (Figure S23). However, it should be pointed out that the interfacial structure is much more complicated than the models we constructed. Due to the limited computational ability, it is difficult to consider all the possibilities of interfacial structures. Combined with the experimental and DFT results, we can still conclude that uniform distribution of nanosized metallic tin in the SnO_2 matrix can generate a lot of more active interfacial sites compared with those of pure SnO_2. Meanwhile, the presence of these active interfacial sites can protect the catalyst from further reduction, as the CO_2 reduction and tin oxide reduction would compete with each other.

4. CONCLUSIONS

In this work, a hybrid precatalyst constructed using SnS_2 and SnO_2 was synthesized based on a synchronous conversion of the SnS precursor. The SnS_2 nanoparticles are uniformly distributed in the structure, which are reduced in prior to SnO_2 under cathodic potential and form metallic Sn nanodomains. The metallic Sn nanodomains are intimately embedded with the SnO_x matrix, forming heterogeneous interfaces on their boundaries. These heterointerfaces induce electron transfer from metallic Sn to SnO_x, which alters catalytic properties and constructs active centers. Consequently, the as-obtained SnS_2@SnO_2 catalyst exhibits a remarkable performance toward the CO_2RR with high selectivity and robust stability. Combining experimental and computational analysis, the mechanism underlying the efficient catalytic performance was proposed.

ASSOCIATED CONTENT

Supporting Information

The Supporting Information is available free of charge at https://pubs.acs.org/doi/10.1021/acsami.2c18522.

Additional experimental and theoretical calculation sections, physical characterization of the SnS precursor, SnS_2@SnO_2 synthesized with different times, and SnO_2 control sample, including XRD patterns, SEM and TEM images, EDS elemental mappings, and XPS measurements, physical characterization of the catalysts after CO_2RR evaluation, CV curves for ECSA calculation, additional electrochemical data in the flow cell, and element ratios by EDS, CO_2RR activity, and selectivity comparison with the previous reports (PDF)

AUTHOR INFORMATION

Corresponding Author

Xiaoxi Huang − *Hoffmann Institute of Advanced Materials, Postdoctoral Innovation Practice Base, Shenzhen Polytechnic, Shenzhen 518055, P. R. China;* orcid.org/0000-0002-1975-2312; Email: xiaoxihuang@szpt.edu.cn

Authors

Zhipeng Liu − *Hoffmann Institute of Advanced Materials, Postdoctoral Innovation Practice Base, Shenzhen Polytechnic, Shenzhen 518055, P. R. China; Shenzhen Institute of Advanced Technology, Chinese Academy of Sciences, Shenzhen 518055, P. R. China*

Chang Liu − *Hoffmann Institute of Advanced Materials, Postdoctoral Innovation Practice Base, Shenzhen Polytechnic, Shenzhen 518055, P. R. China; School of Materials and Metallurgy, University of Science and Technology Liaoning, Anshan 114051, P. R. China*

Suhua Mao − *Hoffmann Institute of Advanced Materials, Postdoctoral Innovation Practice Base, Shenzhen Polytechnic, Shenzhen 518055, P. R. China*

Complete contact information is available at: https://pubs.acs.org/10.1021/acsami.2c18522

Author Contributions

‖Z.L. and C.L. contributed equally to this work.

Notes

The authors declare no competing financial interest.

ACKNOWLEDGMENTS

This study was supported by the Guangdong Natural Science Foundation (2022A1515110034) and Innovation Team Project of Guangdong (2022KCXTD055), the Scientific and Technical Innovation Council of Shenzhen (Task Book No. GXWD20201231165806004, Project No. 20200828014156001).

REFERENCES

(1) Zhu, Z.; Jiang, T.; Ali, M.; Meng, Y.; Jin, Y.; Cui, Y.; Chen, W. Rechargeable Batteries for Grid Scale Energy Storage. *Chem. Rev.* **2022**, *122*, 16610−16751.

(2) Soucy, T. L.; Dean, W. S.; Zhou, J.; Rivera Cruz, K. E.; McCrory, C. C. L. Considering the Influence of Polymer-Catalyst Interactions on the Chemical Microenvironment of Electrocatalysts for the CO_2 Reduction Reaction. *Acc. Chem. Res.* **2022**, *55*, 252−261.

(3) Wang, G.; Chen, J.; Ding, Y.; Cai, P.; Yi, L.; Li, Y.; Tu, C.; Hou, Y.; Wen, Z.; Dai, L. Electrocatalysis for CO_2 conversion: from fundamentals to value-added products. *Chem. Soc. Rev.* **2021**, *50*, 4993−5061.

(4) Tomboc, G. M.; Choi, S.; Kwon, T.; Hwang, Y. J.; Lee, K. Potential Link between Cu Surface and Selective CO_2 Electroreduction: Perspective on Future Electrocatalyst Designs. *Adv. Mater.* **2020**, *32*, No. 1908398.

(5) Daiyan, R.; Saputera, W. H.; Masood, H.; Leverett, J.; Lu, X.; Amal, R.; Disquisition, A. on the Active Sites of Heterogeneous Catalysts for Electrochemical Reduction of CO_2 to Value-Added Chemicals and Fuel. *Adv. Energy Mater.* **2020**, *10*, No. 1902106.

(6) Kibria, M. G.; Edwards, J. P.; Gabardo, C. M.; Dinh, C. T.; Seifitokaldani, A.; Sinton, D.; Sargent, E. H. Electrochemical CO_2 Reduction into Chemical Feedstocks: From Mechanistic Electrocatalysis Models to System Design. *Adv. Mater.* **2019**, *31*, No. 1807166.

(7) Ahmad, T.; Liu, S.; Sajid, M.; Li, K.; Ali, M.; Liu, L.; Chen, W. Electrochemical CO_2 Reduction to C2+ Products using Cu-based Electrocatalysts: A Review. *Nano Res. Energy* **2022**, *1*, No. e9120021.

(8) Han, N.; Ding, P.; He, L.; Li, Y.; Li, Y. Promises of Main Group Metal−Based Nanostructured Materials for Electrochemical CO_2 Reduction to Formate. *Adv. Energy Mater.* **2019**, *10*, No. 1902338.

(9) Nitopi, S.; Bertheussen, E.; Scott, S. B.; Liu, X.; Engstfeld, A. K.; Horch, S.; Seger, B.; Stephens, I. E. L.; Chan, K.; Hahn, C.; Norskov, J. K.; Jaramillo, T. F.; Chorkendorff, I. Progress and Perspectives of Electrochemical CO_2 Reduction on Copper in Aqueous Electrolyte. *Chem. Rev.* **2019**, *119*, 7610−7672.

(10) Cheng, Y.; Hou, P.; Wang, X.; Kang, P. CO_2 Electrolysis System under Industrially Relevant Conditions. *Acc. Chem. Res.* **2022**, *55*, 231−240.

(11) Bushuyev, O. S.; De Luna, P.; Dinh, C. T.; Tao, L.; Saur, G.; van de Lagemaat, J.; Kelley, S. O.; Sargent, E. H. What Should We Make with CO_2 and How Can We Make It? *Joule* **2018**, *2*, 825−832.

(12) Li, X.; Wang, S.; Li, L.; Zu, X.; Sun, Y.; Xie, Y. Opportunity of Atomically Thin Two-Dimensional Catalysts for Promoting CO_2 Electroreduction. *Acc. Chem. Res.* **2020**, *53*, 2964−2974.

(13) Hori, Y.; Wakebe, H.; Tsukamoto, T.; Koga, O. Electrocatalytic Process of CO Selectivity in Electrochemical Reduction of CO_2 at Metal Electrodes in Aqueous Media. *Electrochim. Acta* **1994**, *39*, 1833−1839.

(14) Sun, Y.; Wang, F.; Liu, F.; Zhang, S.; Zhao, S.; Chen, J.; Huang, Y.; Liu, X.; Wu, Y.; Chen, Y. Accelerating Pd Electrocatalysis for CO_2-to-Formate Conversion across a Wide Potential Window by Optimized Incorporation of Cu. *ACS Appl. Mater. Interfaces* **2022**, *14*, 8896−8905.

(15) Zhang, B.; Jiang, Y.; Gao, M.; Ma, T.; Sun, W.; Pan, H. Recent Progress on Hybrid Electrocatalysts for Efficient Electrochemical CO_2 Reduction. *Nano Energy* **2021**, *80*, No. 105504.

(16) Liu, S.; Fan, Y.; Wang, Y.; Jin, S.; Hou, M.; Zeng, W.; Li, K.; Jiang, T.; Qin, L.; Yan, Z.; Tao, Z.; Zheng, X.; Shen, C.; Liu, Z.; Ahmad, T.; Zhang, K.; Chen, W. Surface-Oxygen-Rich Bi@C Nanoparticles for High-Efficiency Electroreduction of CO_2 to Formate. *Nano Lett.* **2022**, *22*, 9107−9114.

(17) Zhai, Y.; Han, P.; Yun, Q.; Ge, Y.; Zhang, X.; Chen, Y.; Zhang, H. Phase Engineering of Metal Nanocatalysts for Electrochemical CO_2 Reduction. *eScience* **2022**, *2*, 467−485.

(18) Jitaru, M. L.; D, A.; Toma, M.; Toma, B. C.; Oniciu, L. Electrochemical Reduction of Carbon Dioxide on Flat Metallic Cathodes. *J. Appl. Electrochem.* **1997**, *27*, 875−889.

(19) Tay, Y. F.; Tan, Z. H.; Lum, Y. Engineering Sn-based Catalytic Materials for Efficient Electrochemical CO_2 Reduction to Formate. *ChemNanoMat* **2021**, *7*, 380−391.

(20) Zhao, S.; Li, S.; Guo, T.; Zhang, S.; Wang, J.; Wu, Y.; Chen, Y. Advances in Sn-Based Catalysts for Electrochemical CO_2 Reduction. *Nano-Micro Lett.* **2019**, *11*, 62.

(21) Feaster, J. T.; Shi, C.; Cave, E. R.; Hatsukade, T.; Abram, D. N.; Kuhl, K. P.; Hahn, C.; Nørskov, J. K.; Jaramillo, T. F. Understanding Selectivity for the Electrochemical Reduction of Carbon Dioxide to Formic Acid and Carbon Monoxide on Metal Electrodes. *ACS Catal.* **2017**, *7*, 4822−4827.

(22) Dutta, A.; Kuzume, A.; Rahaman, M.; Vesztergom, S.; Broekmann, P. Monitoring the Chemical State of Catalysts for CO_2 Electroreduction: An In Operando Study. *ACS Catal.* **2015**, *5*, 7498−7502.

(23) Cheng, Y.; Hou, J.; Kang, P. Integrated Capture and Electroreduction of Flue Gas CO_2 to Formate Using Amine Functionalized SnOx Nanoparticles. *ACS Energy Lett.* **2021**, *6*, 3352−3358.

(24) Fan, L.; Xia, Z.; Xu, M.; Lu, Y.; Li, Z. 1D SnO_2 with Wire-in-Tube Architectures for Highly Selective Electrochemical Reduction of CO_2 to C1 Products. *Adv. Funct. Mater.* **2018**, *28*, No. 1706289.

(25) Yiliguma, Y.; Wang, Z.; Yang, C.; Guan, A.; Shang, L.; Al-Enizi, A. M.; Zhang, L.; Zheng, G. Sub-5 nm SnO_2 Chemically Coupled Hollow Carbon Spheres for Efficient Electrocatalytic CO_2 Reduction. *J. Mater. Chem. A* **2018**, *6*, 20121−20127.

(26) Chen, Y.; Kanan, M. W. Tin Oxide Dependence of the CO_2 Reduction Efficiency on Tin Electrodes and enhanced Activity for Tin/Tin Oxide Thin-Film Catalysts. *J. Am. Chem. Soc.* **2012**, *134*, 1986−1989.

(27) Wu, J.; Risalvato, F. G.; Ma, S.; Zhou, X.-D. Electrochemical Reduction of Carbon Dioxide III. The Role of Oxide Layer Thickness on the Performance of Sn Electrode in a Full Electrochemical Cell. *J. Mater. Chem. A* **2014**, *2*, 1647−1651.

(28) Li, T.; Yang, C.; Luo, J.-L.; Zheng, G. Electrolyte Driven Highly Selective CO_2 Electroreduction at Low Overpotentials. *ACS Catal.* **2019**, *9*, 10440−10447.

(29) Wen, G.; Lee, D. U.; Ren, B.; Hassan, F. M.; Jiang, G.; Cano, Z. P.; Gostick, J.; Croiset, E.; Bai, Z.; Yang, L.; Chen, Z. Orbital Interactions in Bi-Sn Bimetallic Electrocatalysts for Highly Selective Electrochemical CO_2 Reduction toward Formate Production. *Adv. Energy Mater.* **2018**, *8*, No. 1802427.

(30) Dutta, A.; Kuzume, A.; Kaliginedi, V.; Rahaman, M.; Sinev, I.; Ahmadi, M.; Roldán Cuenya, B.; Vesztergom, S.; Broekmann, P. Probing the chemical state of tin oxide NP catalysts during CO_2 electroreduction: A complementary operando approach. *Nano Energy* **2018**, *53*, 828−840.

(31) Baruch, M. F.; Pander, J. E.; White, J. L.; Bocarsly, A. B. Mechanistic Insights into the Reduction of CO_2 on Tin Electrodes using in Situ ATR-IR Spectroscopy. *ACS Catal.* **2015**, *5*, 3148−3156.

(32) Zhang, B.; Guo, Z.; Zuo, Z.; Pan, W.; Zhang, J. The Ensemble Effect of Nitrogen Doping and Ultrasmall SnO_2 Nanocrystals on Graphene Sheets for Efficient Electroreduction of Carbon Dioxide. *Appl. Catal. B* **2018**, *239*, 441−449.

(33) Fang, M.; Zheng, Z.; Chen, J.; Chen, Q.; Liu, D.; Xu, B.; Wu, J.; Kuang, Q.; Xie, Z. Surface Structure-Dependent Electrocatalytic Reduction of CO_2 to C1 Products on SnO_2 Catalysts. *Sustainable Energy Fuels* **2020**, *4*, 600−606.

(34) Li, F.; Chen, L.; Knowles, G. P.; MacFarlane, D. R.; Zhang, J. Hierarchical Mesoporous SnO_2 Nanosheets on Carbon Cloth: A Robust and Flexible Electrocatalyst for CO_2 Reduction with High Efficiency and Selectivity. *Angew. Chem., Int. Ed.* **2017**, *56*, 505−509.

(35) Ye, K.; Zhou, Z.; Shao, J.; Lin, L.; Gao, D.; Ta, N.; Si, R.; Wang, G.; Bao, X. In Situ Reconstruction of a Hierarchical Sn-Cu/SnOx Core/Shell Catalyst for High-Performance CO_2 electroreduction. *Angew. Chem., Int. Ed.* **2020**, *59*, 4814−4821.

(36) He, H.; Wu, J.; Yu, X.; Xia, D.; Wang, Y.; Chen, F.; Wang, L.; Wu, L.; Huang, J.; Zhao, N.; Deng, L.; Liu, Y.-N. Dual-active sites design of Snx-Sby-O-GO nanosheets for enhancing electrochemical

https://doi.org/10.1021/acsami.2c18522
ACS Appl. Mater. Interfaces XXXX, XXX, XXX−XXX

CO_2 reduction via Sb-accelerating water activation. *Appl. Catal. B* **2022**, *307*, No. 121171.
(37) Li, X.; Wang, J.; Lv, X.; Yang, Y.; Xu, Y.; Liu, Q.; Wu, H. B. Hetero-Interfaces on Cu Electrode for Enhanced Electrochemical Conversion of CO_2 to Multi-Carbon Products. *Nano-Micro Lett.* **2022**, *14*, 134.
(38) Gbadamasi, S.; Mohiuddin, M.; Krishnamurthi, V.; Verma, R.; Khan, M. W.; Pathak, S.; Kalantar-Zadeh, K.; Mahmood, N. Interface chemistry of two-dimensional heterostructures - fundamentals to applications. *Chem. Soc. Rev.* **2021**, *50*, 4684−4729.
(39) Li, K.; Xu, J.; Zheng, T.; Zheng, T.; Yuan, Y.; Yuan, Y.; Liu, S.; Liu, S.; Shen, C.; Shen, C.; Jiang, T.; Jiang, T.; Sun, J.; Sun, J.; Liu, Z.; Liu, Z.; Xu, Y.; Xu, Y.; Chuai, M.; Chuai, M.; Xia, C.; Xia, C.; Chen, W. In Situ Dynamic Construction of a Copper Tin Sulfide Catalyst for High-Performance Electrochemical CO_2 Conversion to Formate. *ACS Catal.* **2022**, *12*, 9922−9932.
(40) Lai, Q.; Yuan, W.; Huang, W.; Yuan, G. Sn/SnOx electrode catalyst with mesoporous structure for efficient electroreduction of CO_2 to formate. *Appl. Surf. Sci.* **2020**, *508*, No. 145221.
(41) Liu, Z.; Zhang, J.; Yu, L.; Wang, H.; Huang, X. Thermal Derived Bismuth Nanoparticles on Nitrogen-doped Carbon Aerogel enable Selective Electrochemical Production of Formate from CO_2. *J. CO_2 Util.* **2022**, *61*, No. 102031.
(42) Zhang, J.; Liu, Z.; Guo, H.; Lin, H.; Wang, H.; Liang, X.; Hu, H.; Xia, Q.; Zou, X.; Huang, X. Selective, Stable Production of Ethylene Using a Pulsed Cu-Based Electrode. *ACS Appl. Mater. Interfaces* **2022**, *14*, 19388−19396.
(43) Asadi, M.; Kim, K.; Liu, C.; Addepalli, A. V.; Abbasi, P.; Yasaei, P.; Phillips, P.; Behranginia, A.; Cerrato, J. M.; Haasch, R.; Zapol, P.; Kumar, B.; Klie, R. F.; Abiade, J.; Curtiss, L. A.; Salehi-Khojin, A. Nanostructured Transition Metal Dichalcogenide Electrocatalysts for CO_2 Reduction in Ionic Liquid. *Science* **2016**, *353*, 467−470.
(44) Kresse, G.; Furthmüller, J. Efficient Iterative Schemes for Ab Initio Total-Energy Calculations using a Plane-Wave Basis Set. *Phys. Rev. B* **1996**, *54*, 11169−11186.
(45) Kresse, G.; Furthmüller, J. Efficiency of Ab-Initio Total Energy Calculations for Metals and Semiconductors using a Plane-Wave Basis Set. *Comput. Mat. Sci.* **1996**, *6*, 15−50.
(46) Kresse, G.; Joubert, D. From Ultrasoft Pseudopotentials to the Projector Augmented-Wave Method. *Phys. Rev. B* **1999**, *59*, 1758−1775.
(47) Perdew, J. P.; Burke, K.; Ernzerhof, M. Generalized Gradient Approximation Made Simple. *Phys. Rev. Lett.* **1996**, *77*, 3865−3868.
(48) Grimme, S.; Antony, J.; Ehrlich, S.; Krieg, H.; Consistent, A. and Accurate Ab Initio Parametrization of Density Functional Dispersion Correction (DFT-D) for the 94 Elements H-Pu. *J. Chem. Phys.* **2010**, *132*, No. 154104.
(49) Li, L.; Ozden, A.; Guo, S.; Garci, A. d. A. F. P.; Wang, C.; Zhang, M.; Zhang, J.; Jiang, H.; Wang, W.; Dong, H.; Sinton, D.; Sargent, E. H.; Zhong, M. Stable, Active CO_2 Reduction to Formate via Redox-Modulated Stabilization of Active Sites. *Nat. Commun.* **2021**, *12*, No. 5223.
(50) Klinkova, A.; De Luna, P.; Dinh, C.-T.; Voznyy, O.; Larin, E. M.; Kumacheva, E.; Sargent, E. H. Rational Design of Efficient Palladium Catalysts for Electroreduction of Carbon Dioxide to Formate. *ACS Catal.* **2016**, *6*, 8115−8120.
(51) Wang, V.; Xu, N.; Liu, J.-C.; Tang, G.; Geng, W.-T. VASPKIT: A user-friendly interface facilitating high-throughput computing and analysis using VASP code. *Comput. Phys. Commun.* **2021**, *267*, No. 108033.
(52) Shan, Y.; Li, Y.; Pang, H. Applications of Tin Sulfide-Based Materials in Lithium-Ion Batteries and Sodium-Ion Batteries. *Adv. Funct. Mater.* **2020**, *30*, No. 2001298.
(53) Liu, G.; Li, Z.; Shi, J.; Sun, K.; Ji, Y.; Wang, Z.; Qiu, Y.; Liu, Y.; Wang, Z.; Hu, P. Black Reduced Porous SnO_2 Nanosheets for CO_2 Electroreduction with High Formate Selectivity and Low Overpotential. *Appl. Catal. B* **2020**, *260*, No. 118134.
(54) Kumar, B.; Atla, V.; Brian, J. P.; Kumari, S.; Nguyen, T. Q.; Sunkara, M.; Spurgeon, J. M. Reduced SnO_2 Porous Nanowires with a High Density of Grain Boundaries as Catalysts for Efficient Electrochemical CO_2 -into-HCOOH Conversion. *Angew. Chem., Int. Ed.* **2017**, *56*, 3645−3649.
(55) House, C. I.; Kelsall, G. H. Potential-pH Diagrams for the Sn H_2O-Cl System. *Electrochim. Acta* **1984**, *29*, 1459−1464.
(56) Merino-Garcia, I.; Tinat, L.; Albo, J.; Alvarez-Guerra, M.; Irabien, A.; Durupthy, O.; Vivier, V.; Sánchez-Sánchez, C. M. Continuous Electroconversion of CO_2 into Formate using 2 nm Tin Oxide Nanoparticles. *Appl. Catal. B* **2021**, *297*, No. 120447.
(57) Jin, S.; Hao, Z.; Zhang, K.; Yan, Z.; Chen, J. Advances and Challenges for the Electrochemical Reduction of CO_2 to CO: From Fundamentals to Industrialization. *Angew. Chem., Int. Ed.* **2021**, *60*, 20627−20648.
(58) Jiang, H.; Luo, R.; Li, Y.; Chen, W. Recent Advances in Solid−Liquid−Gas Three-Phase Interfaces in Electrocatalysis for Energy Conversion and Storage. *EcoMat* **2022**, *4*, No. e12199.

https://doi.org/10.1021/acsami.2c18522
ACS Appl. Mater. Interfaces XXXX, XXX, XXX−XXX